CONF-9607145--2

SAND96-2071C
SAND--96-2071C

Amplitude and phase beam characterization using a two-dimensional wavefront sensor

Daniel R. Neal, W. J. Alford, James K.Gruetzner
Sandia National Laboratories, Org. 1128, PO Box 5800, Albuquerque, NM 87185-1423

Mial E. Warren
Sandia National Laboratories, Org. 1312, PO Box 5800, Albuquerque, NM 87185-0603

ABSTRACT

We have developed a two-dimensional Shack-Hartman wavefront sensor that uses binary optic lenslet arrays to directly measure the wavefront slope (phase gradient) and amplitude of the laser beam. This sensor uses an array of lenslets that dissects the beam into a number of samples. The focal spot location of each of these lenslets (measured by a CCD camera) is related to the incoming wavefront slope over the lenslet. By integrating these measurements over the laser aperture, the wavefront or phase distribution can be determined. Since the power focused by each lenslet is also easily determined, this allows a complete measurement of the intensity and phase distribution of the laser beam. Furthermore, all the information is obtained in a single measurement. Knowing the complete scalar field of the beam allows the detailed prediction of the actual beam's characteristics along its propagation path. In particular, the space-beamwidth product, M^2, can be obtained in a single measurement. The intensity and phase information can be used in concert with information about other elements in the optical train to predict the beam size, shape, phase and other characteristics anywhere in the optical train. We present preliminary measurements of an Ar^+ laser beam and associated M^2 calculations.

Keywords: wavefront sensor, microlens arrays, diffractive optics, binary optics, laser beam characterization, M^2, Shack-Hartmann sensor, laser beam diagnostics, beam quality.

1 Introduction.

In many instances where a laser beam is needed, it is important to know something about the laser beam quality. The beam quality affects how the beam will propagate, as well as how tightly it will focus. Unfortunately, beam quality is a somewhat elusive concept. Numerous attempts have been made to define beam quality, stretching back almost to the invention of the laser.[1,2] In practice, any one of these measures will have some flaw in certain situations, and many different measures are often used. Among these is the M^2 parameter (space-beamwidth product).[1,3]

The intensity and phase distribution of a laser beam are sufficient for determining how the beam will propagate or how tightly it can be focused. Most of the beam quality measurements rely on characterizing the beam from only the intensity distribution, since obtaining this is a comparably straightforward process. However, if both the intensity and phase distribution could be obtained simultaneously, then all the information would be available from a single measurement.

In general, phase is measured with an interferometer. Interferometers are sensitive instruments that have been extensively developed.[4] They can be used to measure laser beams by using a shearing or filtered Mach-Zehnder arrangement, and can produce the desired intensity and phase distribution. Unfortunately, these systems rapidly become complex, and are slow and unwieldy, as well as being expensive.

A Shack-Hartmann wavefront sensor is an alternative method for measuring both intensity and phase.[5] Such sensors have been developed by the military for defense adaptive optics programs over the last 25 years.[4–6] This sensor is a simple de-

vice that is capable of measuring both intensity and phase distributions in a single frame of data. The advent of micro-optics technology for making arrays of lenses has allowed these sensors to become much more sophisticated in recent years. In addition, advances in CCD cameras, computers and automated data acquisition equipment have brought the cost of the required components down considerably. With a Shack-Hartmann wavefront sensor it is relatively straightforward to determine the intensity and phase of a beam. This allows not only the derivation of various beam quality parameters, but also the numerical propagation of the sampled beam to another location, where various parameters can then be measured.

M^2 has become a commonly used parameter to generally describe near-Gaussian laser beams. It is especially useful in that it allows a prediction of the real beam spot size and average intensity at any successive plane using simple analytic expressions. This allows system designers the ability to know critical beam parameters at arbitrary planes in the optical system. Unfortunately, measuring M^2 is somewhat difficult. To date, obtaining M^2 has generally required measurements of intensity distributions at multiple locations along the beam path. Although efforts have been made to obtain this parameter in a single measurement,[7] this still suffers from the need to make simultaneous measurements at more than one location. The technique presented here requires a single measurement at a single location.

In succeeding sections, we will describe how a wavefront sensor is constructed along with preliminary experimental data. A method for computing M^2 will be developed and applied to various simulated and real beams.

2 Wavefront sensor design and analysis.

2.1 Beam characteristics from a single measurement and location.

The time-independent electric field of a coherent light beam directed along the z-axis can in general be described by its complex amplitude profile,

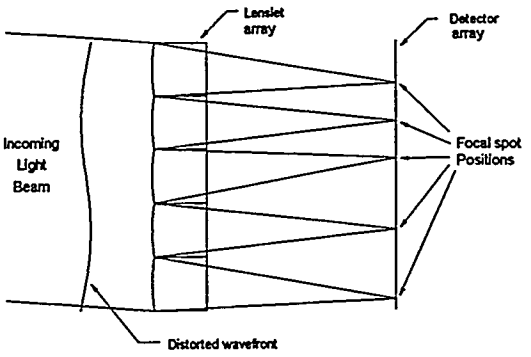

Figure 1: Basic configuration of a wavefront sensor.

$\tilde{E}(x,y;z) = \left|\tilde{E}(x,y;z)\right| \exp\left[i\phi(x,y;z)\right]$, where ϕ is referenced to the wavefront phase on the z-axis. Due to rapid temporal oscillations at optical frequencies, it is not possible to directly measure the electric field. However, by using a Shack-Hartmann wavefront sensor, one can indirectly reconstruct a discrete approximation to the electric field at a given plane normal to the z-axis.

A Shack-Hartmann sensor provides a method for measuring the phase and intensity of an incident light beam. The sensor is based on a lenslet array that splits the incoming light into a series of subapertures, each of which creates a focus on a detector (usually a CCD camera). (See Figure 1.) The wavefront of the incoming beam is defined as a surface that is normal to the propagation direction of the light. Hence distorted light will have a wide collection of propagation directions and the separate lenslets will focus the light into different positions on the detector. By determining the position of each of these focal spots the wavefront slope over the lenslet can be measured. The wavefront itself must be reconstructed by integrating these wavefront slope measurements.

There are several steps in wavefront sensor data reduction. First the sensor is placed in a reference beam and data is acquired with a camera for calibration. Since there are a large number of focal spots in the field, the image must be divided into a set of small windows, each centered on a focal spot peak, with one window per lenslet. Once the windows have been found, a centroid is computed

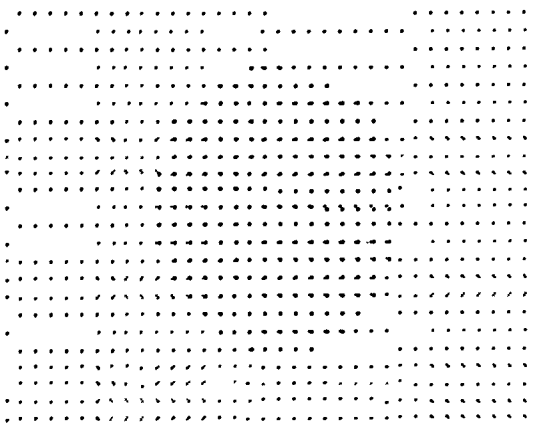

Figure 2: Image of data from Shack-Hartmann sensor. Centroid positions calculated from image. The light gray spots are the centroid positions of the calibration beam.

using a center-of-mass algorithm:

$$\rho_{x,l} = \frac{\sum_{(i,j)\in W_l} I_{ij} x_i}{\sum_{(i,j)\in W_l} I_{ij}}. \qquad (1)$$

With pixels indicated by the i,j indices, a sum is made over the pixels in each window (W_l, where l indicates a particular lenslet) of the intensity-weighted locations. (When not mentioned explicitly, similar equations hold for the y-axis.) This results in a calibration set of centroids, $\rho_{x,l}\big|_{CAL}$ and $\rho_{y,l}\big|_{CAL}$. The sensor has now been completely calibrated and is ready for acquisition and measurement of actual data. Note that the calibration beam need not be a collimated beam, as long as its characteristics are known; results are then deviations from this reference.

The first step in analyzing real data is the same as that for the calibration data. The data is acquired and digitized and then centroids are computed using the windows calculated in the calibration step. A typical image is shown in Figure 2. Once these centroids have been obtained, and with the lenslet to CCD distance, L, known, the wavefront slopes can be calculated:

$$\theta_{x,l} = \frac{\partial \phi}{\partial x_l} = \frac{\rho_{x,l} - \rho_{x,l}\big|_{CAL}}{L}. \qquad (2)$$

Figure 3 displays an example of this calculation for an expanding beam.

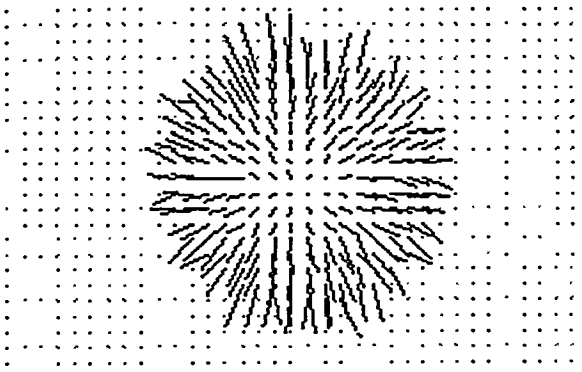

Figure 3: Vector plot displaying wavefront slopes of an expanding beam.

The final step is the wavefront reconstruction. This is the solution of the gradient equation,

$$\vec{\nabla}\phi = \frac{\partial \phi}{\partial x}\,\hat{\imath} + \frac{\partial \phi}{\partial y}\,\hat{\jmath}\,, \qquad (3)$$

where the data provides sampled values for the wavefront gradient,

$$\left.\frac{\partial \phi}{\partial x}\right|_l = \theta_{x,l} \quad \text{and} \quad \left.\frac{\partial \phi}{\partial y}\right|_l = \theta_{y,l}. \qquad (4)$$

Here θ_x and θ_y are the measured slope data. The reconstruction proceeds by finding a set of ϕ_l values that obey the above equations. Commonly used methods include least-squares procedures and marching methods.[6]

One method that has advantages in that it takes account of the intensity distribution as well as the phase slopes is known as the modal reconstructor method. In this method the data is fit to the derivatives of an analytical surface described by an expansion in terms of a set of basis functions. One simple case is the use of a polynomial expansion. Thus the phase ϕ might be described by

$$\phi = a_{00} + a_{10}x + a_{01}y + a_{11}xy + \cdots + a_{ij}x^i y^j. \qquad (5)$$

This description uses normal polynomials in x and y. We have also used different basis sets, such as Hermite and Zernike functions. The derivatives of the phase are then easily determined by

$$\frac{\partial \phi}{\partial x} = a_{10} + a_{11}y + 2a_{20}x + \cdots + i a_{ij} x^{i-1} y^j\,, \qquad (6)$$

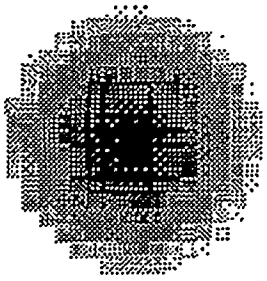

Figure 4: Phase map for Ar+laser beam, with tilt removed. Curvature dominates the phase structure.

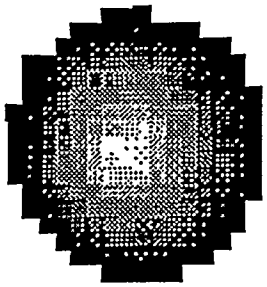

Figure 5: Intensity map for an Ar+ laser.

with a similar expression for the y-derivative. Equation 6 is then fit to the wavefront slope data using a least-squares method. Since equation (5) determines the wavefront phase in terms of these a_{ij} (with an arbitrary constant of integration, a_{00}, which is set equal to zero), the complete wavefront has been determined. Figures 4 and 5 illustrate a typical phase and intensity distribution obtained by this method.

The above provides a complete measurement of the beam intensity and phase, sampled by the lenslets. This measure is from a single time and location. It can be used for calculation of other parameters of interest, such as M^2 as shown in the next section. In addition, the reconstructed wavefront can be propagated to another location using a standard propagation code (e.g., LightPipes©[8] or GLAD©[9]).

2.2 M^2 from a single measurement point.

One commonly used parameter for characterizing laser beam quality is the space-beamwidth product, or M^2 parameter.[1] Let the complex electrical field distribution of a beam directed along the z-axis be given by $\tilde{E}(x,y,z)$, with the corresponding spatial frequency domain description of the beam, $\tilde{P}(s_x,s_y,z)$ given by its Fourier transform, $\tilde{P}(s_x,s_y,z) = \Im\left\{\tilde{E}(x,y,z)\right\}$. Beam intensities in each domain are then defined by $I(x,y,x) \equiv \left|\tilde{E}(x,y,z)\right|^2$ and by $\hat{I}(s_x,s_y,z) \equiv \left|\tilde{P}(s_x,s_y,z)\right|^2$. The M^2 parameter is then defined by:

$$M_x^2 = 4\pi\sigma_{x_o}\sigma_{s_x} \tag{7}$$

where σ_{x_o} is intensity standard deviation at the beam waist (z_{x_0}) in the x-direction, defined by

$$\sigma_x^2(z) \equiv \frac{\iint (x-\bar{x})^2 I(x,y,z)\,dxdy}{\iint I(x,y,z)\,dxdy} \tag{8}$$

and σ_{s_x} the spatial-frequency standard deviation of the beam along the x-axis

$$\sigma_{s_x} = \frac{\iint (s_x-\bar{s}_x)^2 \hat{I}(s_x,s_y)\,ds_x ds_y}{\iint \hat{I}(x,y,z)\,ds_x ds_y}. \tag{9}$$

Note that $\sigma_{s_x}^2$ is not a function of z, and can be obtained using the Fourier transform of the electric field.

(The first moments of the beam along the x-axis and the s_x-axis are indicated by $\bar{x}$ and $\bar{s}_x$, respectively. The spot size of the beam is $w_x(z) \equiv 2\sigma_x$. The corresponding y-axis quantities hold for σ_{y_o}, σ_{s_y}, etc., *mutatis mutandis*, throughout this paper. In addition, the normalizing factor in the denominators shall be indicated by $\mathcal{P} = \iint I(x,y,z)\,dxdy = \iint \hat{I}(x,y,z)\,ds_x ds_y$.))

In the case of a paraxial beam in the z-direction, with an arbitrary reference plane (z_1), it has been shown by Siegman[10] that the intensity standard deviation will have an axial distribution given by,

$$\begin{aligned}\sigma_x^2(z) &= \sigma^2(z_1) - A_{x,1}\times(z-z_1) \\ &\quad + \lambda_{s_x}^2\sigma_{s_x}^2\times(z-z_1)^2\end{aligned} \tag{10}$$

where $A_{x,1}$ is given by the function

$$A_x(z_1) = \frac{\lambda}{\pi \mathcal{P}} \iint_{-\infty}^{\infty} dx\, dy\, x \times \left|\tilde{E}\right|^2 (x,,y,z_1) \frac{\partial \phi(x,y,z_1)}{\partial x}. \quad (11)$$

(We have followed Siegman in suppressing the phase tilt term.) The beam waist, or location of minimum intensity variance, is obtained from equation (10):

$$(z_{x_0} - z_1) = \frac{A_{x,1}}{2\lambda^2 \sigma_{s_x}^2}. \quad (12)$$

Substituting back into Equation (10) yields the relationship

$$\sigma_{x_o}^2 \equiv \sigma_x^2(z_{x_0}) = \sigma^2(z_1) - \frac{A_{x,1}^2}{4\lambda^2 \sigma_{s_x}^2}. \quad (13)$$

M_x^2 follows immediately from equation (7).

It should be noted that equations (13) and (11) are not derived from series expansions in the vicinity of the beam waist, but are analytical derivations dependent only upon the paraxial wave equation, the paraxial propagation assumption, and the Fourier transform relationships between the complex electric field amplitude ($\tilde{E}(x,y,z)$) and the spatial-frequency beam description ($\tilde{P}(s_x,s_y,z)$).

As shown in section 2.1, it is possible to obtain a discrete description of the beam electric field amplitude and phase in a given plane normal to the z-axis. As part of the measuring process, discrete values for $\frac{\partial \phi}{\partial x}$ and $\frac{\partial \phi}{\partial y}$ are also obtained. By means of the above formulæ and standard numerical integration techniques one can then obtain values for M^2 and the waist locations, $z_{0x,y}$.

The sequence is as follows. (See Figure 6.) From the Shack-Hartmann sensor, the distribution of intensity, $I(x,y,z_1)$ and wavefront slope, $\frac{\partial \phi}{\partial X}$ and $\frac{\partial \phi}{\partial y}$ are obtained. From these, the electric field, $\tilde{E}(x,y,z_1) = E(x,y,z_1)\exp[i\phi(x,y,z_1)]$ is calculated. The spatial-frequency electric field distribution, $\tilde{P}(s_x,s_y,z_1)$, is derived using a Fourier transform algorithm, such as the fast Fourier transform (FFT). From these the intensity distributions in both domains, $I(x,y,z_1)$ and $\hat{I}(s_x,s_y,z_1)$, are obtained, whence numerical values for the variances, $\sigma_x^2(z_1)$ and $\sigma_{s_x}^2$, are calculated. Concurrently, the integral of equation (11) is computed, with the

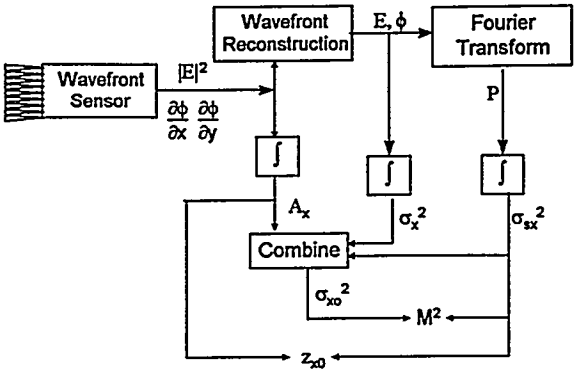

Figure 6: Computing waist location and M^2 in a single measurement. The Shack-Hartmann sensor gives a set of wavefront slopes and intensities; these are used to reconstruct an electric field wavefront (normalized to zero phase on the z-axis). The spatial frequency field is obtained by Fourier transform. Application of other relationships described in the text yield waist location and the M^2 parameter.

results being used in equations (13) and (12) to produce the waist location and intensity variance. The waist intensity standard deviation and the spatial-frequency standard deviations immediately yield the M^2 parameter per equation (7).

2.3 Algorithm sensitivity.

In order to determine the sensitivity of the algorithms developed in Section 2.2, a number of different modelled beams were created. This allowed for a check on the algorithm with known conditions, without having to consider the effects of noise or experiment errors. To this end, the laser beam was modelled with either a Gaussian or sech^2 intensity profile, and the effect of various parameters was considered. The modelled beam was broken into the appropriate samples to model the lenslet array and detector, and the equations of section 2.1and 2.2 were used to determine M^2. For calculations to obtain beam characteristics, the integrals in Equations (8), (9), and (11) are replaced with discrete sums over validly measured values. All Fourier transforms are performed using standard discrete Fourier transform methods, and the fast Fourier transform (FFT) algorithm when

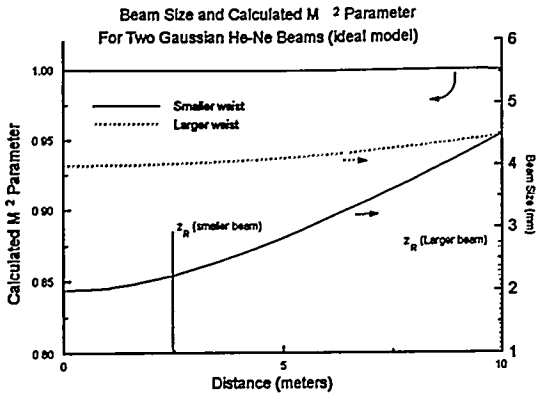

Figure 7: For both modeled beams, the calculated M^2 parameter is unity throughout the range of propagation.

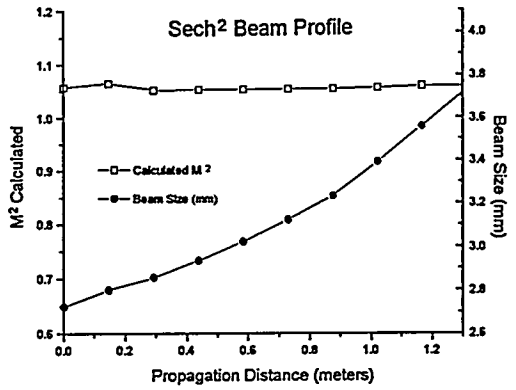

Figure 8: Algorithm performance for with hyperbolic secant squared beam. Modeled beam propagated using LightPipes©.

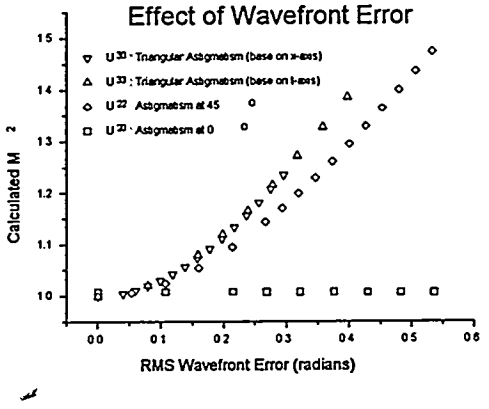

Figure 9: Effect on M^2 for various levels of selected aberrations.

possible. All calculations were performed using a standard numerical computation software package (MATLAB[14]) on standard desktop computers.

Initial results with modeled Gaussian beams have been very encouraging. Elliptical Gaussian beams were modeled, adjusted in piston by setting the phase equal to zero on the z-axis. Figure 7 details the results of modeling two Gaussian beams of differing waist size. For these beams, the M^2 parameter is unity. The smaller beam was propagated over several Rayleigh ranges, and the larger over a full Rayleigh range. In each case the algorithm correctly calculated the M^2 parameter based solely on a sampling of the wavefront at a given (but unknown to the algorithm) distance from the waist. A similar computation was conducted with a Gaussian beam with a constant 1.3 milliradian tilt, or roughly one wave across the beam diameter. Again the algorithm correctly calculated a value of unity for the M^2 parameter throughout the range tested.

The model was also tested on non-Gaussian beam profiles. Figure 8 depicts the results for a beam with a hyperbolic secant squared intensity profile, which has a theoretical M^2 of 1.058. The beam was modeled with a flat phase front at $z = 0$, simulating a beam waist, and then propagated over the distance shown (roughly one Rayleigh range) using LightPipes©.[8]

As another check on the algorithm, beams with various levels and types of aberration were examined, as shown in Figure 9 (M_x^2 values are shown). Four types of aberration were examined, based upon four Zernike polynomial aberration functions[4]: astigmatism with axis at $\pm 45°$ (U_{20}), astigmatism with axis at 0° or 90° (U_{22}); triangular astigmatism with base on x-axis (U_{30}); and triangular astigmatism with base on y-axis (U_{33}). The algorithm correctly calculated an M^2 value near unity for U_{22} (or $y^2 - x^2$) astigmatism, as well as showing increasing values of M^2 for increased U_{20} ($2xy$), U_{30} ($3xy^2 - x^3$), and U_{33} ($y^3 - 3x^2y$) astigmatism.

Of concern in the use of this method is the granularity of the reconstructed wavefront and the effect this would have on the computation of M^2. This was tested by examining the results of the algorithm when sampling a modeled Gaussian beam

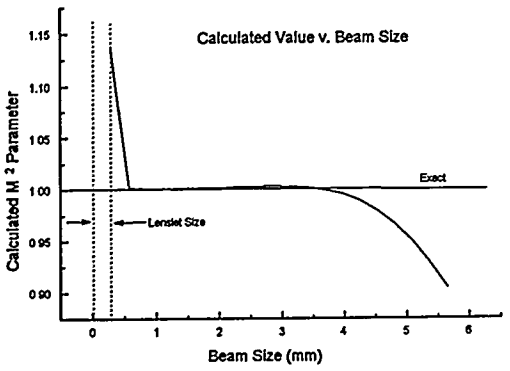

Figure 10: Gaussian beam modeled at waist; M^2 calculation for a detector consisting of a 40 x 32 array of lenslets, each 250μm on a side. Once detectable beam energy no longer falls on the detector, there is a loss of intensity in the higher spatial frequencies, resulting in a decrease in the M^2 parameter.

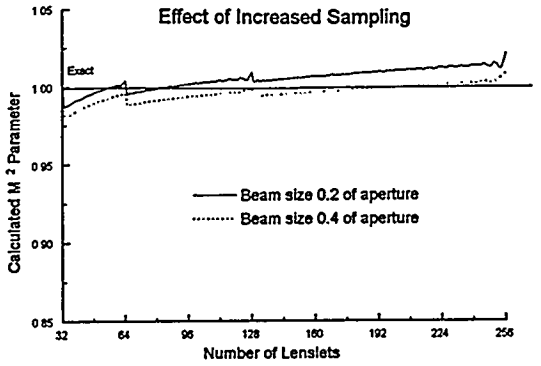

Figure 11: Effect of increasing the number of lenslets across the aperture.

at the waist. The algorithm correctly calculated the M^2 parameter once information was available from several lenslets. Accuracy remained within a few percent until the beam size (2σ) reached about 45% of the total aperture. (See Figure 10.) At this point, in a zero noise environment, detectable energy from the beam just reaches to the edge of the aperture. Thus all beam energy outside the aperture is below the sensitivity threshold of the detector. However, once energy which would otherwise be detectable fell outside of the detector aperture, the value of the M^2 parameter determined by the algorithm drops. We also found, as shown in Figure 11, that there was no need to go to an extreme number of lenslets in order to obtain good results in a low-noise environment. It is important to note that this set of results are for a Gaussian beam at the waist, and as a result there were no beam aberrations. Further analysis is needed to examine the behavior of the algorithm for other conditions. We expect that the algorithm should correctly calculate M^2 as long as the spatial structure of the aberration is larger than twice the lenslet spacing.

3 Experimental measurement.

3.1 Wavefront sensor design.

Shack-Hartmann wavefront sensors have been used for many years as sensors for adaptive optics in military high energy laser and atmospheric compensation. However, recently they have been applied to measurement applications in thermal flow, turbulence and surface measurement.[11] While these early sensors were one dimensional in order to make high bandwidth measurements, recently fully two dimensional sensors have been developed.[5,12]

One of the chief limitations on making wavefront sensors is the fabrication of an appropriate lenslet array. Early lenslet arrays were either individually ground and polished lens segments that were assembled together, or were fabricated with step and repeat processes. With the advent of diffractive (or binary) optics technology, the methods for fabricating lenslet arrays have greatly improved.

Diffractive optics technology is the application of integrated circuit manufacturing technology to the fabrication of optics. Photolithography and etching are used to create the desired lens surface profile as described in Figure 12. The basic steps are as follows:

1. The design of the optic is developed using a

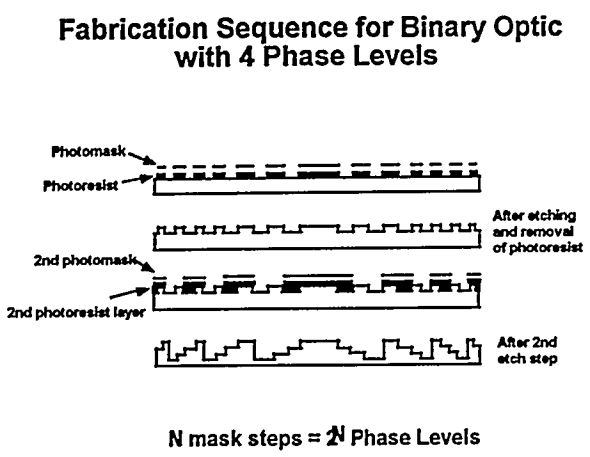

Figure 12: Fabrication sequence for binary optics.

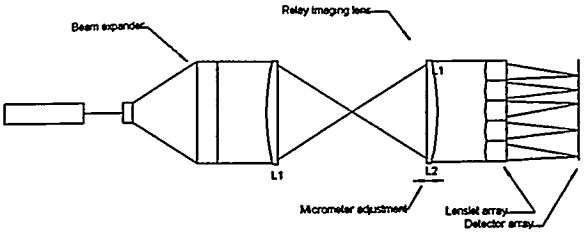

Figure 13: Test setup for calibrating wavefront sensor. The second lens, L2, is adjusted to provide different amounts of wavefront curvature to the sensor.

series of computer programs to describe the desired lenslet shape and profile. These include a code to define the shape and placement that solves the exact Huygens-Fresnel equations, a diffractive analysis code, and a photomask layout tool for lens array placement.

2. Photomasks are fabricated that discretize the desired surface profile into a number of levels. With four masks, this will result in sixteen levels (2^N). These masks are typically e-beam written directly from the data.

3. A thin layer of photoresist is spun onto the fused silica substrate.. The mask pattern is transferred to this layer by uv contact or projection lithography. Once the photoresist is developed this results in the desired pattern in photoresist on the substrate.

4. The substrate is etched in an anisotropic etch system to a precise depth. Thus the mask pattern is transferred into the substrate.

5. The process of steps 2-4 is repeated for each mask with each successive etch being twice the depth of the preceding etch. This will build up the profile to the required shape.

With this technology extremely high precision lens arrays can be made. They have an extremely precise surface profile, with features down to 1 micrometer and 100% fill factor. Furthermore, they can be arranged in many different configurations to compensate for other effects in the optical system.[13]

The only other needed equipment to make a wavefront sensor is a CCD camera. We have used off-the-shelf cameras because of their low cost, and have found that they yield excellent results. The camera is interfaced to a frame grabber for data acquisition into the computer. Once data is acquired, the analysis proceeds along the lines described in section 2.1.

3.2 Lenslet positioning procedure.

In addition to the wavefront calibration discussed in Section 2.1, the lenslet-to-CCD distance, L in equation (2), must be determined experimentally. To accomplish this objective, we used an optical system as shown in Figure 13 to introduce various amounts of wavefront curvature in a known fashion. In this arrangement we used a pair of Spindler and Hoyer 250 mm focal length achromats space 2f apart. By adjusting the position of the second achromat slightly (with a micrometer driven translation stage) we were able to obtain data with known curvature as shown in Figure 14. It is important to note that, even though we used high quality achromats, there was significant residual wavefront error on the resulting image due to the finite aberrations of the lens pair. Ray-tracing analysis and experiment verified that about 2.5 waves of error were expected. This error was dealt with by conducting the wavefront sensor calibration (Section 2.1) with light that had pass through the same lenses at exactly 2f spacing.

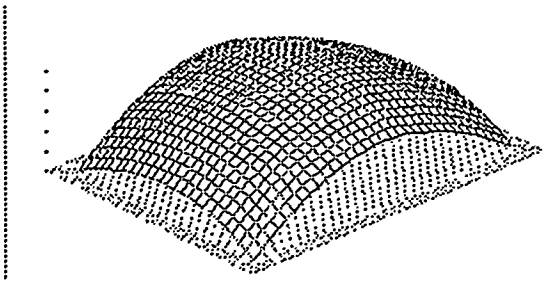

Figure 14: Curved wavefront measured with wavefront sensor for a 60m radius of curvature wavefront.

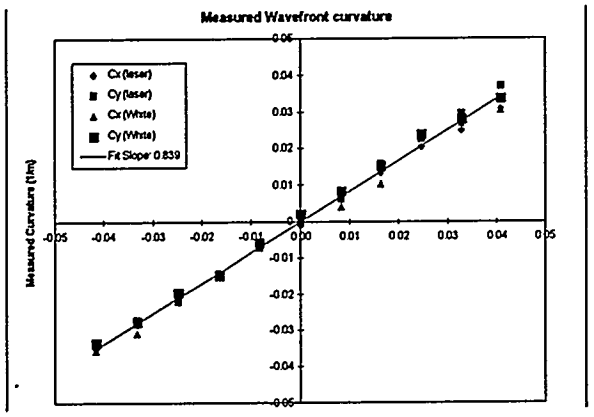

Figure 15: Position of lenslet array using both white light and laser light sources. The slope error reprents a displacement of the lenslet array by 4 mm from the nominal focal plane.

Data was acquired with different lens pair spacing as a function of the position of lens 2. A summary of this data is presented in Figure 15, as a plot of measured wavefront curvature verses input curvature. This plot is not exactly linear: the variations are due to variations in the real wavefront caused by the finite aberrations of the lens pair. The slope of this line is related to the exact distance between the lenslet array and the detector. Using this information, this distance was adjusted to produce an exact match between nominal lens focal length and camera to lens spacing. Setting $L = f$ (where f is the lenslet focal length) produces the smallest spot size, allowing the largest dynamic range on the sensor. This positioning procedure allowed for an accurate determination of L. The post-positioning data is shown on Figure 16.

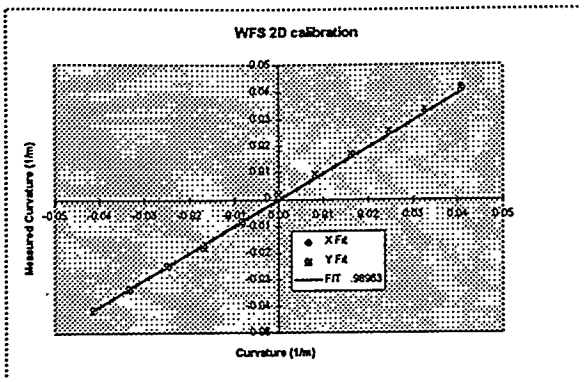

Figure 16: The lenslet position after adjustment. The slope of near unity indicates the lenslet array is positioned one focal length from the detector.

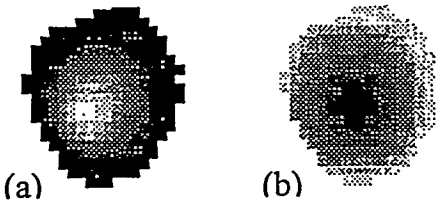

Figure 17: Display of Ar+ beam measured with wavefront sensor. (a) Beam intensity. (b) Beam phase.

3.3 Laser beam measurement

Once the wavefront sensor was calibrated, a series of laser beams were measured to experimentally determine M^2. The reference beam was an expanded, collimated HeNe laser. The laser source was an Ar+ laser that was approximately 2 m away from the detector. This laser was chosen because it had intracavity aperture and alignment adjustments that would allow us to produce aberrated beams. Figure 17 is an example of an aberrated beam intensity and phase distribution measured with the wavefront sensor. In this case the laser was deliberately misaligned. The algorithms developed previously predicts an M_x^2 of 3.73 and an M_y^2 of 5.09; the RMS wavefront error is 0.11 um. A number of data sets were taken where the laser current, beam power, and cavity alignment were varied to produce various quality beams. Representative data is tabulated in Figure 18.

In this table, the M^2 values are calculated in

Laser Parameters	M^2_x	M^2_y
Aperture 204 Current: 20A	2.97	3.94
Aperture 204 Current: 20A	2.99	3.88
Aperture 355 (full open) Current: 25A Horizontal misalignment	2.64	4.02
Aperture 355 (full open) Current: 25A More misalignment	3.29	5.47
Aperture 150 Current: 25A Misaligned as above	3.73	5.09

Figure 18: Calculated M^2 obtained from various Ar+ laser beams.

both the x and y directions. The initial entries are for relatively good beams, but with a large intracavity aperture setting. The two separate calculations of the M^2 parameters of the laser under the same operating conditions are consistent with each other, indicating the repeatability of the measurements. For the last three entries, the beam was deliberately misaligned to produce an aberrated beam. The M^2 values reflect this, and show the evolution of the misalignment compared to the initial settings.

In all cases, the M^2 parameters are higher than expected based upon the smooth spatial profiles of the beams. No independent method of M^2 measurement was available when the data were taken. The higher than expected values are most likely due to noise in the wings, which have a large effect on second moment calculations. Additionally, noise in the spatial domain affects the Fourier transform, and can result in increased values at the higher spatial frequencies in the spatial-frequency domain. Analysis of these problems is in the initial stages; current results are discussed in section 2.3.

4 Conclusions

We have developed a 2D wavefront sensor that is capable of obtaining detailed intensity and phase values from a single measurement. This sensor is based on a microlens array that is built using binary optics technology to provide fine sampling and good resolution. We have developed a method for calculating M^2. Since the full beam intensity and phase distribution is known, a complete beam intensity and phase distribution can be predicted anywhere along the beam.

We have used this sensor to analyze various laser beams, calculate M^2, and propagate a beam. Calculated values of M^2 are believed to be high for unestablished reasons. Further work includes determination of the noise characteristics of the sensor, and an evaluation of the effects of noise and other errors for both real and simulated beams.

Using this sensor a laser can be completely characterized and aligned. The user can immediately tell if the beam is single or multimode, and can predict the spot size and full intensity and phase distribution at any plane in the optical system. The sensor is easy to use, simple, robust and low cost.

5 Acknowledgments.

This work supported by the U.S. Department of Energy, under Contract number DE-AC04-94AL 85000.

6 REFERENCES

[1] A.E. Siegman, "New developments in laser resonators" SPIE Vol.1224, Optical Resonators (1990), pp.2-14.

[2] H. Weber, "Some historical and technical aspects of beam quality" *Opt.Quant.Elec.* 24 (1992), S861-S864.

[3] M.W. Sasnett, and T.F. Johnston, Jr., "Beam characterization and measurement of propagation attributes" SPIE Vol. 1414, Laser

Beam Diagnostics (1991), pp. 21-32.

[4] D. Malacara, ed., *Optical Shop Testing*, John Wiley & Sons, Inc., 1982.

[5] D. Kwo, G. Damas, W. Zmek, "A Hartmann-Shack wavefront sensor using a binary optics lenslet array," SPIE Vol. 1544, pp. 66–74 (1991).

[6] W.H. Southwell, "Wave-front estimation from wavefront slope measurements," *JOSA* **70** (8), pp.993-1006 (August, 1980).

[7] J.A. Ruff and A.E. Siegman, "Single-pulse laser beam quality measurements using a CCD camera system" Appl.Opt., Vol.31, No.24 (20 Aug. 92) pp.4907-4908.

[8] Gleb Vdovin, *LightPipes: beam propagation toolbox*, ver.1.1, Electronic Instrumentation Laboratory, Technische Universiteit Delft, Netherlands, 1996.

[9] *General Laser Analysis and Design (GLAD) code*, v. 4.3, Applied Optics Research, Tucson, AZ, 1994.

[10] A.E. Siegman, "Defining the Effective Radius of Curvature for a nonideal Optical Beam" *IEEE J. Quant.Elec.*, Vol.27, No.5 (May 1991), pp. 1146-1148.

[11] D.R. Neal, T.J. O'Hern, J.R. Torczynski, M.E. Warren and R. Shul, "Wavefront sensors for optical diagnostics in fluid mechanics: application to heated flow, turbulence and droplet evaporation," SPIE Vol. 2005, pp. 194–203 (1993).

[12] L. Schmutz, "Adaptive optics: a modern cure for Newton's tremors," Photonics Spectra (April 1993).

[13] D.R. Neal, J.D. Mansell, J.K Gruetzner, R. Morgan and M.E. Warren, "Specialized wavefront sensors for adaptive optics," SPIE Vol. 2534, pp. 338–348 (1995).

[14] MATLAB for Windows, v. 4.2c.1, The MathWorks, Inc., Natick, MA, 1994.